Simulation of the Intraseasonal Variations of the Indian Summer Monsoon in a Regional Coupled Ocean–Atmosphere Model

VASUBANDHU MISRA

Center for Ocean-Atmospheric Prediction Studies, and Department of Earth, Ocean and Atmospheric Science, and Florida Climate Institute, Florida State University, Tallahassee, Florida

AKHILESH MISHRA

Florida Climate Institute, Florida State University, Tallahassee, Florida, and Center for Ocean-Atmospheric Science and Technology, Amity University Rajasthan, Jaipur, India

AMIT BHARDWAJ

Center for Ocean-Atmospheric Prediction Studies, and Florida Climate Institute, Florida State University, Tallahassee, Florida

(Manuscript received 27 June 2017, in final form 28 December 2017)

ABSTRACT

This paper describes a novel simulation of active and break spells of the Indian summer monsoon (ISM) using a relatively high-resolution regional coupled ocean–atmosphere climate model (RCM) run at 10-km grid spacing. Similar to what is seen in observations, the RCM-simulated active (break) spells are characterized by stronger (weaker) rainfall over central India and anomalous low-level atmospheric flow that enhances (weakens) the climatological flow pattern. Highlights of this study include the improved spatiotemporal structure, propagation characteristics, and amplitude of the intraseasonal variations of the ISM rainfall in the RCM simulation as compared with some of the more recent simulations conducted with global models at coarser spatial resolutions. This study's RCM simulation also displays associated variations in the upper ocean, with active (break) spells of the ISM coinciding with colder (warmer) sea surface temperatures (SSTs) in both the Arabian Sea and the Bay of Bengal. These SST anomalies are mainly sustained by corresponding net heat flux anomalies on the ocean surface. The active (break) spells are further associated with shoaling (deepening) of the mixed layer depth, which is critical for the SST response to heat flux. All of these simulated features of intraseasonal variations of the ISM have been seen in earlier observational studies, which further confirms the fidelity of the model simulation and the importance of coupled air–sea interactions and upper-ocean stratification.

1. Introduction

Intraseasonal variations (ISVs) are a dominant feature of the Indian summer monsoon (ISM); they are characterized by a higher amplitude of variation than what is typically seen in interannual variations (Webster et al. 1998; Krishnamurthy and Kinter 2003; Waliser 2006). ISVs of the ISM occur over a wide time span (from 20 to 90 days) that overlaps with the time period of the Madden–Julian oscillation of the boreal winter season (Yasunari 1979; Raghavan et al. 1975; Krishnamurti and Subrahmanyam 1982; Wang and Rui 1990). The ISVs of the ISM are characterized by active and break phases of rainfall, wherein the former is above the seasonal mean and the latter is below the seasonal mean (Krishnamurthy and Shukla 2000). Sikka and Gadgil (1980) found these contrasting phases typically include a northward propagation of cloud bands beginning at the equatorial Indian Ocean and ending near to the foothills of the Himalayas in northern India. In addition to this northward propagation, Lawrence and Webster (2002) noted an eastward propagation of convection in the equatorial Indian Ocean. And through composite analysis, they found that when the eastward propagation of convection was weak, the northward translation of an ISV was also correspondingly weak. Further, the authors asserted that this was consistent with the propagation of equatorial waves that elicit surface frictional convergence into the low pressure

Corresponding author: Vasubandhu Misra, vmisra@fsu.edu

DOI: 10.1175/JCLI-D-17-0434.1

center of the Rossby wave mode and that the propagation consequently forced the northward movement of ISVs (Wang and Xie 1997; Lawrence and Webster 2002).

Despite our increased understanding of ISVs over the years, their simulations by general circulation models continue to display significant bias, albeit with modest improvements over the years (Sperber and Annamalai 2008; Lin et al. 2008; Jiang et al. 2011; Abhik et al. 2016; Krishnamurthy 2016). For example, Lin et al. (2008) indicated that models from phase 3 of the Coupled Model Intercomparison Project (CMIP) overestimated the equatorial Indian convection and underestimated the northward propagation of ISVs. When comparing these results with CMIP5 models, Sperber et al. (2013) concluded that the northward propagation of ISVs was significantly improved. However, CMIP5 models continued to display significant bias in the observed northwest–southeast-tilted rainband associated with ISVs. Similarly, Krishnamurthy (2016) showed a clear improvement in ISV simulations in the more recent version of the operational seasonal climate forecast model of the National Centers for Environmental Prediction as compared to the center's previous version. Furthermore, several studies have shown that models with an interactive ocean simulate the northward propagation of ISVs, which are otherwise generated as a standing mode in the atmosphere-only (with prescribed SST) integrations (Wang et al. 2009; Sharmila et al. 2013). And thus, there is growing consensus that air–sea interaction improves simulation with higher fidelity and extends prediction skill of ISVs (Waliser et al. 2001; Wang et al. 2009; Sharmila et al. 2013; Roxy et al. 2013).

In addition to global general circulation models, there has been expanded use of regional climate models to simulate the ISM (Dash et al. 2006; Raju et al. 2015; Umakanth et al. 2016; Misra et al. 2017). In general, these studies claim that regional climate models offer higher resolution relative to general circulation models, which enables better representation of the land–sea coastlines, orography, and land cover, all of which lead to some modest improvements of the spatial and temporal variations of simulated ISMs. More recently, Ham et al. (2016) suggested that air–sea interaction resolved in a regional coupled ocean–atmosphere model improved the simulation of the East Asian summer monsoon. In this study, we utilize a regional coupled ocean–atmosphere model (RCM) that is forced at the lateral boundaries by global reanalysis datasets. This model setup run at 10-km grid resolution provides us with the unique ability to understand upper-ocean responses to ISVs. Unlike some of the observational studies conducted with limited field observations or disparate observational datasets that include potentially independent errors (e.g., Sengupta et al. 2001; Bhat 2002; Parampil et al. 2010), the simulation discussed in this paper provides a dynamically consistent dataset of the atmospheric and oceanic variables. Some recent observational studies have indicated the existence of prominent intraseasonal variations of the upper-ocean heat content in the Bay of Bengal (BoB; Sengupta and Ravichandran 2001; Vecchi and Harrison 2002; Krishnamurti et al. 2017). These studies have given us a broader understanding of ISVs. For example, Sengupta et al. (2001) and Bhat (2002) indicated a basinwide warming of the BoB SST (nearly 1°C) prior to onset of the active phase of the ISM. Similarly, Li et al. (2017) suggested that when either the barrier layer thickness (BLT) or mixed layer depth (MLD) is large, intraseasonal SST anomalies tend to be weak in the BoB.

The purpose of this study is to present the ISV results from a climate simulation conducted at an unprecedented grid resolution of 10 km for both the atmosphere and ocean component of a regional climate model. In the following section, we briefly describe the model and the experimental setup. This is followed by a description of the model diagnostics conducted. The results are discussed in section 4, followed by our conclusions, which are discussed in section 5.

2. Model description and experiment design

We use the Regional Spectral Model (RSM; atmospheric component)–Regional Ocean Modeling System (ROMS; oceanic component) as our RCM (Li and Misra 2014; Misra et al. 2017). This RCM was recently used to simulate the ISM by Misra et al. (2017). A brief outline of the RSM and ROMS is provided in Table 1. No flux correction is applied to the RCM simulation. For this study, the RSM and ROMS are situated on identical grids (at 10-km grid resolution) so that there is direct exchange of atmospheric fluxes to ROMS and SST to RSM without any interpolation. The coupling interval for the exchange between RSM and ROMS is three hours. The domain used in this study for the RCM integration is depicted in Fig. 1. The RCM is laterally forced by the National Centers for Environmental Prediction–Department of Energy global atmospheric reanalysis (Kanamitsu et al. 2002) at a 6-h interval and the Simple Ocean Data Assimilation, version 2.2.4 (SODA), global oceanic analysis (Carton and Giese 2008) at a monthly interval for the atmospheric (RSM) and oceanic (ROMS) components, respectively. The RCM integration is for a period of 10 years (1986–95).

3. Methodology for model diagnostics

To isolate the ISV from observations and model simulation, we use the fourth-order, bandpass, recursive Butterworth time filter (Guillemin 1957), which has been widely used for extracting intraseasonal signals of the

TABLE 1. A brief outline of the RCM.

	Reference
Atmospheric model (RSM)	
Twenty-eight (28) vertical-terrain-following sigma levels with double sine–cosine series with wall boundary conditions as basis functions for horizontal discretization	Juang and Kanamitsu (1994)
Deep convection	Moorthi and Suarez (1992)
Shallow convection	Tiedtke (1983)
Clouds	Zhao and Carr (1997)
Boundary layer	Hong and Pan (1996)
Land model	Ek et al. (2003)
Gravity wave drag	Alpert et al. (1988)
Longwave radiation	Chou et al. (1999)
Shortwave radiation	Chou and Suarez (1994)
Ocean model (ROMS)	
Thirty (30) vertical sigma levels on horizontal staggered Arakawa C grid	Haidvogel et al. (2000); Shchepetkin and McWilliams (2005)
Mixing scheme	Mellor and Yamada (1982); Umlauf and Burchard (2003)
Boundary layer formulation	K profile (Large et al. 1994)

ISM (Krishnamurti and Subrahmanyam 1982; Goswami et al. 1998; Misra et al. 2012). The time filtering is conducted at individual grid points for the entire model domain, with a bandpass of 20–90 days. We also make composites of active (dry) spells of the ISM over the RCM simulation period by isolating periods of five successive days of 20–90-day filtered positive (negative) precipitation anomalies over central India (15°–25°N and 75°–85°E), following Goswami and Xavier (2003). The observational datasets used in the verification are outlined in Table 2. It should be noted that the observational period does not overlap with the model simulation period (e.g., precipitation, SST) for some of the datasets. This is not expected to hinder our analysis as we are examining the ISV phenomenology with a focus on the upper-ocean features in the RCM and not on the interannual or other lower-frequency variations.

4. Results

a. Seasonal climatology

Figures 1a and 1b show the observed mean June–September (JJAS) climatology of rainfall and 850-hPa winds from observations and the RCM simulation, respectively. Rainfall climatology is calculated using the Tropical Rainfall Measuring Mission, version 3B43 (TRMM-3B43; Huffman et al. 2010), data, while the source of the 850-hPa wind analysis is the Modern-Era Retrospective Analysis for Research and Applications, version 2 (MERRA-2) (Molod et al. 2015; Gelaro et al. 2017). Overall, the large-scale pattern of rainfall in the RCM simulation is reasonably well captured. The observed rainfall maximum along the Western Ghats, northeast India, and the Indo-Chinese peninsula contrasted with semiarid regions of the Indian Deccan Plateau and the northwest regions are simulated in the RCM. Similarly, the observed 850-hPa southwesterlies over the Arabian Sea (AS) gradually leading to the monsoon trough residing over central India and the northern BoB is also apparent in the RCM simulation. However, it should be noted that the observational analysis of rainfall and winds are approximately 2.5 and 5 times coarser in spatial resolution than in the RCM simulation. As a result, we observe sharper rainfall gradients in the RCM simulation near steep orography (e.g., Western Ghats, Himalayas, and the Purvanchal Mountains in northeast India) and between the semiarid and moist regions of the domain. Furthermore, Shige et al. (2017) indicate that infrared-based rainfall estimates tend to show erroneous smearing of rainfall in the coastal oceans upstream of the Western Ghats and Arakan Yoma region of Myanmar due to detection of cold brightness temperatures associated with extensive cirrus anvils. However, the TRMM Precipitation Radar shows that rainfall maxima occur over the upslope of the Western Ghats and the Arakan Yoma (Shige et al. 2017) as simulated in the RCM (Fig. 1b). The bias of the RCM simulation is also apparent in Fig. 1, with the underestimation (overestimation) of rainfall over BoB (central India) and an overestimation of the rainfall along the southern and eastern boundaries of the regional domain.

Similarly, Fig. 2 shows the temperature stratification of the upper ocean from reanalysis and the RCM simulation. As noted in some of the earlier observational studies, the thermal stratification of the northern Indian Ocean plays an important role in the manifestation of the intraseasonal SST anomalies (Waliser et al. 2004; Li et al. 2016, 2017). The shallower MLD in the BoB makes the SST in the region more responsive to changes in the

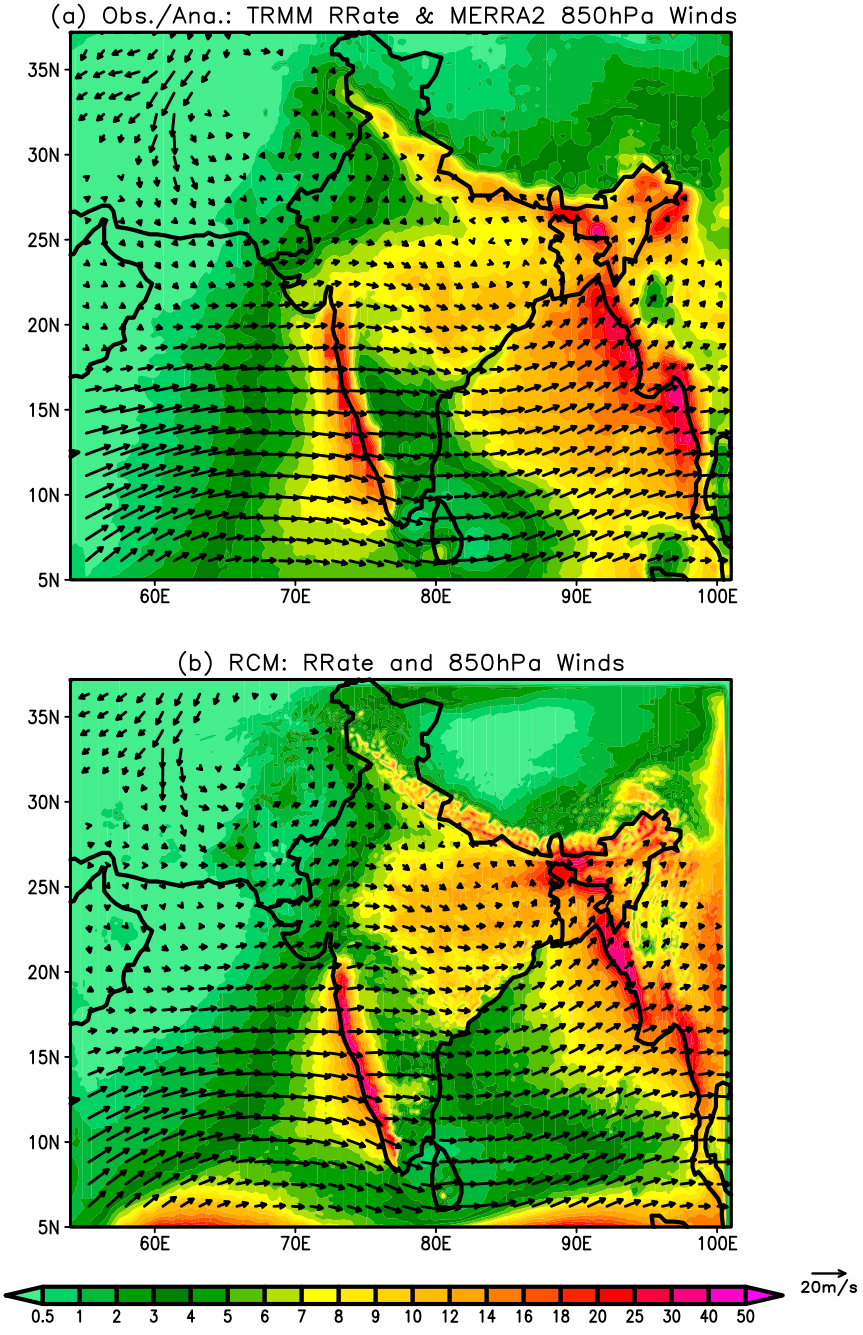

FIG. 1. JJAS climatology of 850-hPa winds (vectors; m s^{-1}) and rainfall (colors; RRate; mm day^{-1}) from (a) observations and (b) RCM.

atmospheric fluxes compared to the AS (Rao et al. 2011; Roxy et al. 2013). Therefore, the intraseasonal variations are more significant in the BoB during the ISM season (Sengupta and Ravichandran 2001; Rao et al. 2011; Krishnamurti et al. 2017). The intraseasonal anomalies in the AS are found to be strongest in the early (May–June) and decaying (September–October) stage of the ISM season (Li et al. 2016). The observed large-scale features of relatively shallow MLD in the BoB and the northern AS (Fig. 2a) are well captured in the RCM simulation (Fig. 2b). Similarly, the relatively larger MLD over the southwestern AS is also simulated in the RCM simulation, albeit with a bias of a shallower depth. It should be noted that MLD bias in the RCM, both over the BoB and the AS, differs from many other recent global models that tend to simulate with a bias

TABLE 2. Verification datasets used in the study.

	Variable	Source	Reference	Remarks
1	Daily precipitation	TRMM-3B43	Huffman et al. (1995, 1997); Adler et al. (2000)	Available for 1998–2015 at 0.25° × 0.25° grid
2	Daily 850-hPa winds and atmospheric fluxes	MERRA-2	Molod et al. (2015); Gelaro et al. (2017)	Available for 1979–present at 0.5° × 0.625° grid
3	Daily SST	OSTIA	Donlon et al. (2012)	Available for 2006–present at 5 km × 5 km
4	Monthly depth of the 26°C isotherm (proxy for ocean heat content)	SODA	Carton and Giese (2008)	Available for 1958–2001 at 0.25° × 0.4°
5	Monthly upper-ocean currents and temperature			

of a thicker MLD (Roxy et al. 2013; Akhil et al. 2014; Li et al. 2016). Roxy et al. (2013) suggested that such seasonal bias in the MLD is a potential source of errors in the forecasting of ISVs. The depth of the 26°C isotherm (Fig. 2c), which represents the tropical cyclone heat potential (Shay et al. 2000), and the depth of the 20°C isotherm (Fig. 2e), which is a proxy for upper-ocean heat content of the tropical oceans, show comparatively deeper depths in the AS as compared to the BoB. This feature is also represented in the RCM simulation but with a bias of shallower depths in both basins (Figs. 2d,f).

b. *Intraseasonal variations of precipitation*

The intraseasonal variance of precipitation and 850-hPa winds from observations and RCM are shown in Figs. 3a and 3b. The model-simulated intraseasonal variance seems reasonable, showing the highlighted regions of precipitation variance along the western coast of India and the Myanmar coast. Likewise, the wind variance is much stronger in the central and eastern parts of India (Indo-Gangetic and Brahmaputra Plains) in both the observations and the model analysis. Figure 3a also reveals a dominance of zonal wind variations in the Indo-Gangetic Plains, while in central India and the BoB the variance of the meridional component of the winds becomes equally significant. These features of the ISV are reasonably well simulated in the RCM simulation (Fig. 3b). Furthermore, the low intraseasonal variance region in the oceanic regions around Sri Lanka are also very well captured by the model simulation. That said, there are apparent discrepancies in the RCM simulation that include an underestimation of the precipitation variance over the BoB and an overestimation of precipitation variance over central and northern India.

A composite analysis of the dry and wet spells of the ISM is shown in Fig. 4. Both in the observations and in the RCM simulation, the dry and wet spells of the ISM are characterized by corresponding precipitation anomalies across central India and the BoB with anomalous anticyclonic and cyclonic circulations at 850 hPa, respectively. Furthermore, in comparing the wind anomalies of the intraseasonal time scales in Fig. 4 with the corresponding wind climatology in Fig. 1, it is apparent that the dry (wet) spells imply strengthening (weakening) of the prevalent westerlies over the northern BoB. This has been widely observed in earlier studies (e.g., Krishnamurti et al. 1992; Krishnamurthy and Shukla 2007). The precipitation anomalies are more widespread across the BoB than in the AS, in both the observations and the simulation (Fig. 4). However, the RCM in comparison to the observations underestimates the anomalies of precipitation and 850-hPa wind anomalies over the BoB while overestimating it over the Indo-Gangetic Plains. This RCM simulation can be considered quite reasonable given the current state-of-the-art global model bias at intraseasonal time scales of the ISM (Lin et al. 2008; Neena et al. 2017).

The composite power spectrum of central India rainfall for the 18 and 10 seasons of the Tropical Rainfall Measuring Mission dataset and the RCM simulation is shown in Figs. 5a and 5b, respectively. The bump in the observed spectral density between 20 and 90 days (Fig. 5a) is also seen in the RCM simulation (Fig. 5b), with a slightly larger amplitude but also within the uncertainty range of the observed spectral estimates. The peak intraseasonal power is around 40 days (Figs. 5a,b), which is consistent with the findings of Krishnamurthy and Shukla (2000, 2007).

c. *Propagation characteristics*

To show the propagation characteristics of the intraseasonal variations, we display the lag regression of zonally averaged (70°–95°E), bandpass (20–90 days)-filtered precipitation anomalies on the corresponding bandpass-filtered precipitation anomalies over central India in Figs. 6a and 6b from both TRMM observations and the RCM simulations, respectively. The meridional northward propagation of the precipitation anomalies from the equatorial latitudes to northern India is quite

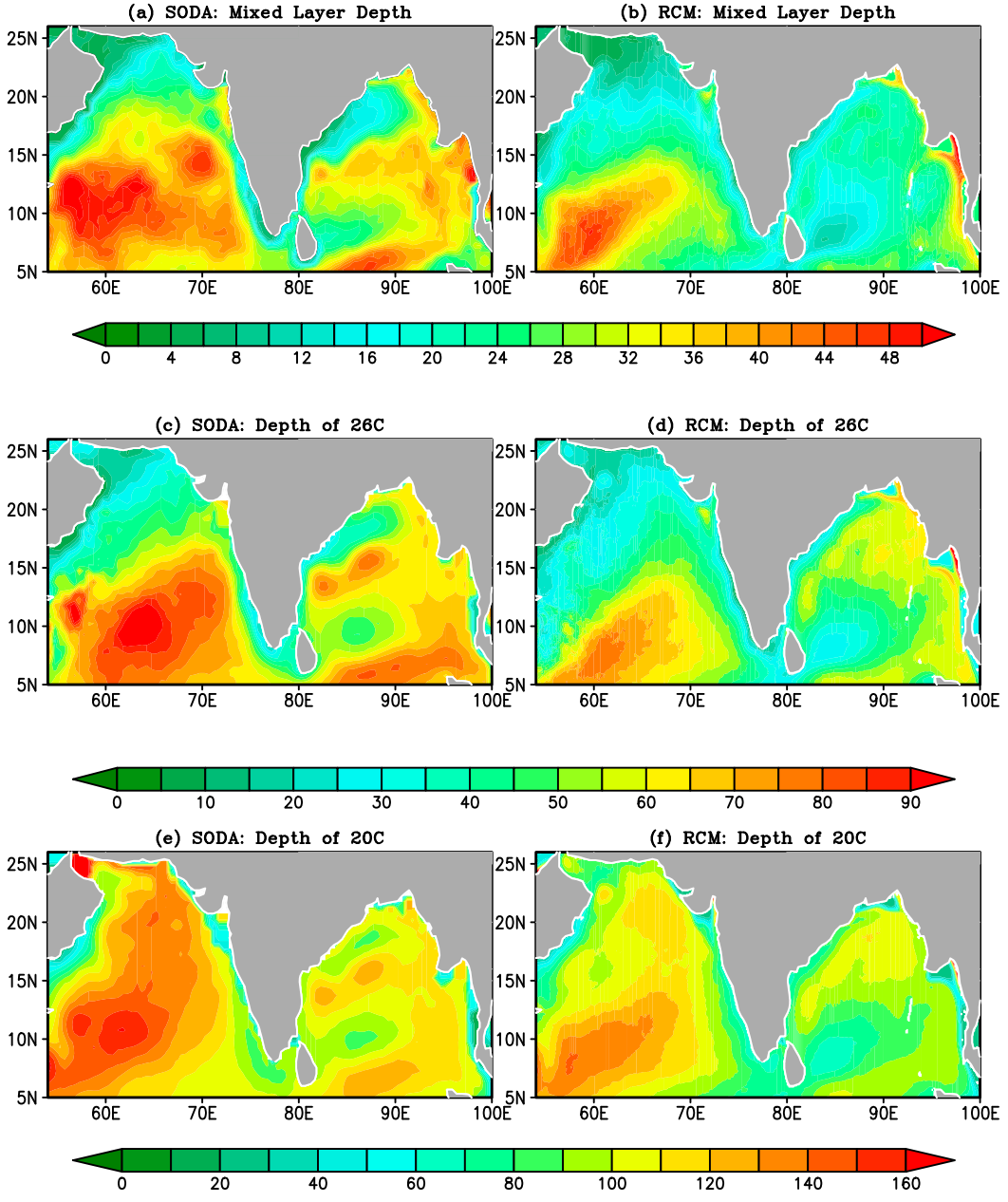

FIG. 2. JJAS climatology of depth (m) of (a),(b) MLD and the (b),(c) 26°C and (d),(e) 20°C isotherms from (left) observations and (right) RCM.

apparent in both the observations and the model simulation. The stronger amplitude of the regression coefficients in the RCM simulation (Fig. 6b) is striking. However, the RCM (Fig. 6b) represents slightly faster propagation with a broader temporal variation than the observations (Fig. 6a). This feature of faster propagation of the ISV in the RCM is contrary to many of the global models, which simulate a much slower-propagating ISV than observed meridional propagation (Wang et al. 2009; Sharmila et al. 2013). Additionally, the model tends to propagate the anomalies farther north, beyond 27°N, while the observations seem to halt just beyond 24°N. Some of these differences between the RCM simulation and the observations shown in Fig. 6 become far more apparent and clear in Fig. 7. Similar to Fig. 6, in Fig. 7 we show the regression of the filtered precipitation anomalies on the corresponding filtered precipitation anomalies over central India at different leads and lags. The weaker precipitation anomalies of the RCM simulation over the BoB relative to the observations are

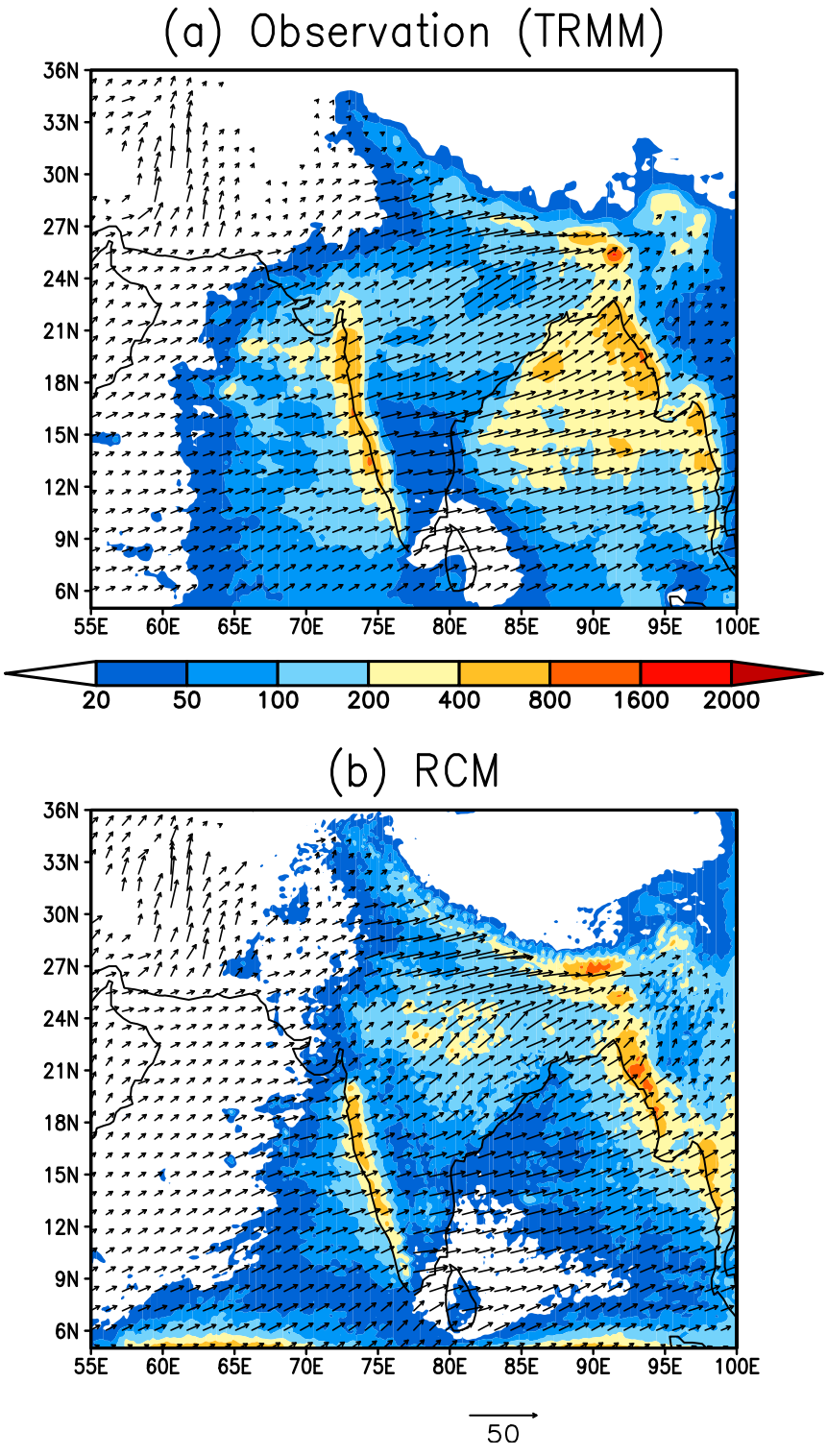

FIG. 3. Intraseasonal (20–90 days) variance of precipitation (color shaded; $mm^2\ day^{-2}$) and 850-hPa winds (vectors; $m^2\ s^{-2}$) from (a) observations and (b) RCM. The vectors represent the variance of the zonal and meridional wind components.

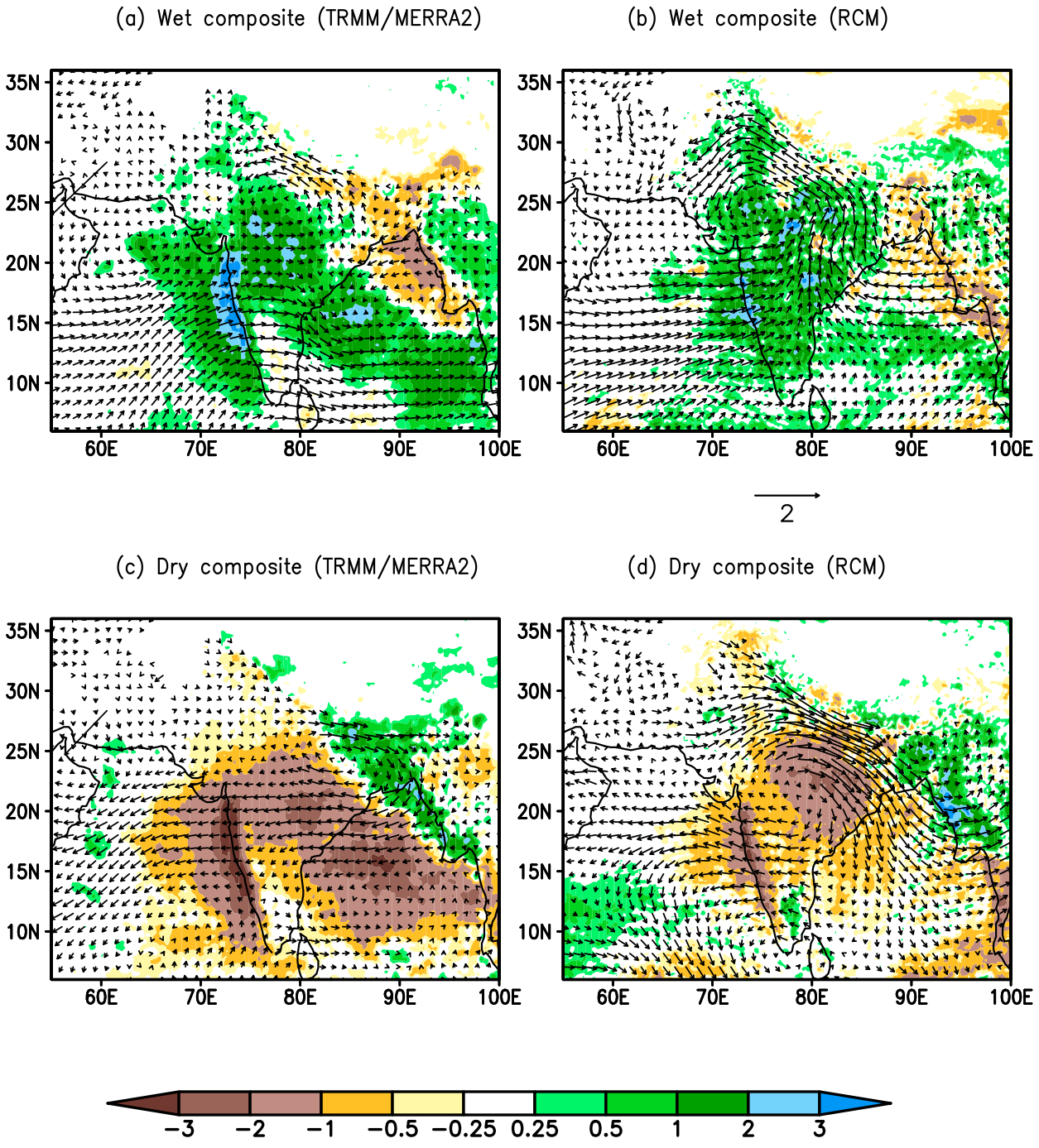

FIG. 4. The composite intraseasonal (20–90-day bandpass filtered) 850-hPa winds (vectors; m s^{-1}) and rainfall (color shaded; mm day^{-1}) from (a),(c) observations and (b),(d) RCM.

quite apparent at all lags (Fig. 7). But over land, especially along the western Ghats and central India, they are very comparable. Furthermore, the northwest–southeast tilt of the precipitation anomalies from northwest India to the BoB is also comparable in both observations and the RCM simulation. The successful tilted feature of the ISV simulated by the RCM is a feature that has been found to be difficult to simulate in many of the global models (Sperber et al. 2013). It may be noted that in all Fig. 7 panels the central India rainfall anomaly is flanked in both the southern and northern directions with rainfall

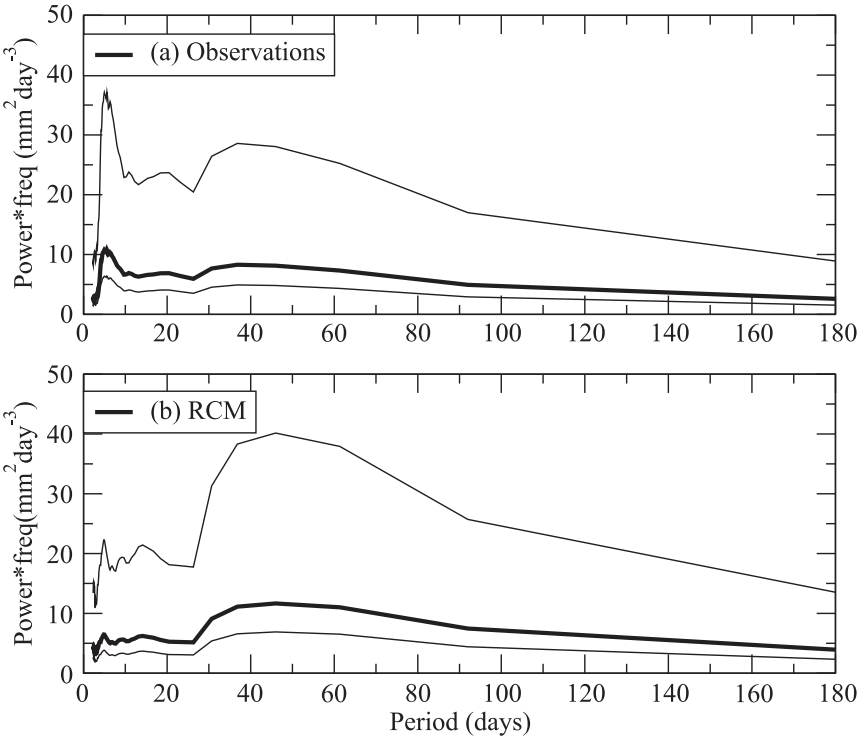

FIG. 5. The sample spectrum (thick lines) of central Indian (15°–25°N and 75°–85°E) rainfall from (a) TRMM observations and (b) the RCM simulation. The thin lines represent the 95% confidence interval according to a chi-squared test for 20 degrees of freedom.

anomalies of the opposite sign, suggestive of its meridional propagating feature.

d. Intraseasonal anomalies of the ocean surface

Having verified some of the rainfall and lower-tropospheric circulation characteristics of the ISV in the RCM simulation, we now analyze the associated surface and subsurface ocean variations in the simulation. The RCM simulation at 10 km in a coupled ocean–atmosphere framework gives us a unique perspective on the evolution of the ISV in the surrounding oceans. In Figs. 8a and 8b we show the standard deviation of the intraseasonal (20–90-day filtered) SST anomalies from the operational sea surface temperature and sea ice analysis (OSTIA; see Table 2) and the RCM simulation, respectively. The strong variations along the western edge of the regional domain, across the Gulf of Oman, and along the peninsular coast of India with a minimum in the equatorial latitudes of the northern Indian Ocean are well captured in the RCM. The RCM simulation's comparatively weaker anomalies in the northern BoB and the AS are also noted (Fig. 8b).

In Fig. 9, we show the wet and dry intraseasonal composites based on central India rainfall for SST and all of the heat flux terms. This figure reveals a broad picture, whereby that during active (inactive) periods of the ISM, SST anomalies appear slightly colder (moderately warmer) in the BoB and over the AS (Figs. 9a,b). This type of ISV of the SST during active and nonactive spells of the ISM over BoB has been noted in other observational studies (Sengupta and Ravichandran 2001; Bhat 2002).

In Fig. 9, the SST anomalies are asymmetrical with dry spells showing a larger anomaly than the wet spells. This was also observed during the BoB Monsoon Experiment (BOBMEX; Bhat 2002). We argue later in this paper that this feature is a result of a corresponding asymmetry in the ocean subsurface. Nonetheless, corresponding net heat flux anomalies broadly show more heat flux leaving the ocean surface during wet spells (Fig. 9c) compared to the dry spells (Fig. 9d) [i.e., negative (positive) values of net heat flux over regions of cold (warm) SST anomaly regions]. In the observational analysis of Parampil et al. (2010) it was suggested that intraseasonal variations of the BoB SST is largely a response to net heat flux.

Interestingly and contrary to observational studies (Bhat 2002), there are fewer latent heat flux anomalies coming off the surface of the ocean during the wet spell (Fig. 9e) than during the dry spell (Fig. 9f). This is likely a manifestation of the dry bias of the RCM

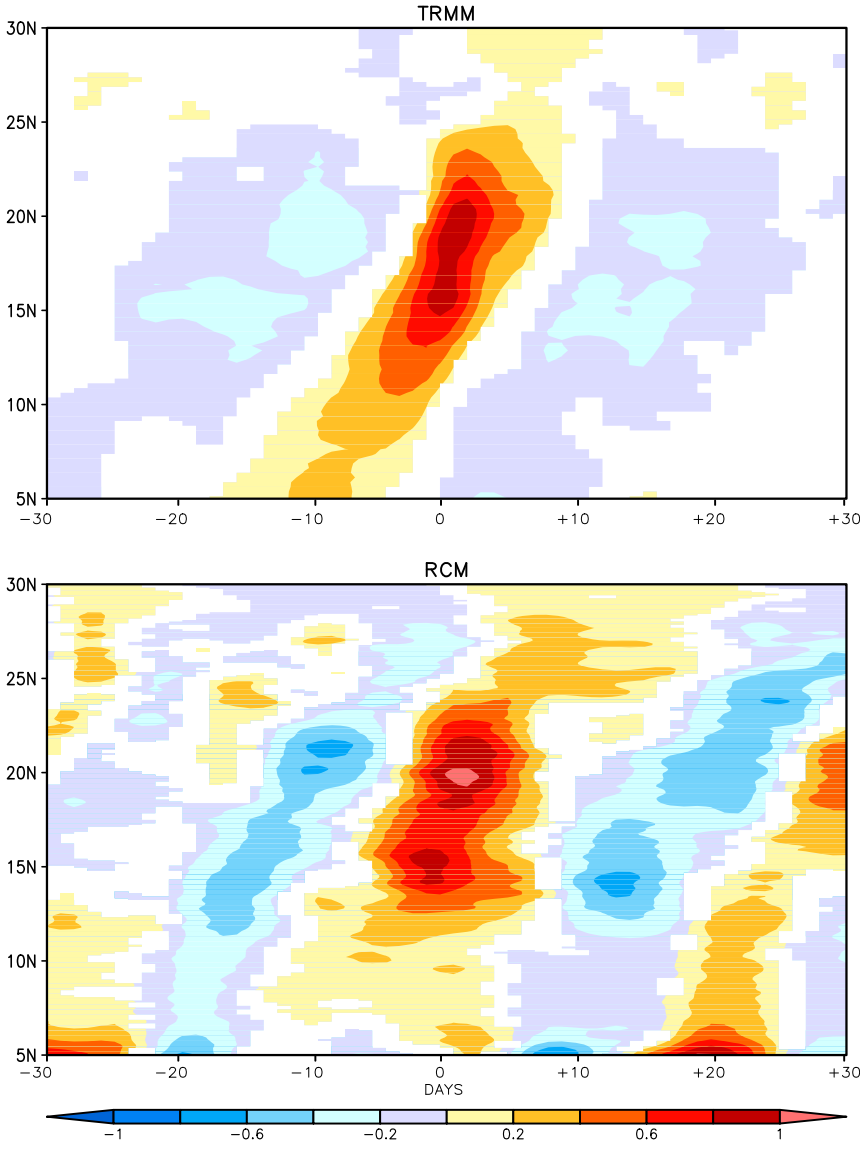

FIG. 6. The regression of zonally averaged, 20–90-day bandpass-filtered rainfall between longitudes of 70° and 95°E on the corresponding 20–90-day filtered precipitation anomalies over central India (75°–85°E and 15°–25°N) from the (a) observations (TRMM) and (b) RCM simulation. The abscissa is the lag in days with negative (positive) lags suggesting that central Indian rainfall anomalies lead (lag) the zonally averaged rainfall anomaly. Only values significant at the 95% confidence interval according to a *t* test are plotted.

simulation over the BoB on the intraseasonal time scales (Fig. 4). It should be noted, however, that some of these observational studies have been conducted with very limited sample sizes. For example, in Bhat (2002) the analysis was over one active and one inactive period within a month of the ISM. Similarly, Parampil et al. (2010) conducted their observational study over the BoB from three Argo floats. In Fig. 9, we are showing a composite of far more events over a 10-yr period at a uniform 10-km grid spacing. And, as indicated earlier, the intraseasonal wet composite wind anomalies weaken over the northern BoB, which will likely force a weakening of the enthalpy fluxes. Although the sensible heat flux anomalies (Figs. 9g,h) are much smaller than the latent heat flux, their signs are similar with respect to the active and inactive periods of ISM.

The anomalies of the shortwave flux in Figs. 9i,j further indicate that this component of the heat flux is reduced in wet spells compared to dry spells of the ISM. These anomalies of the shortwave flux are consistent

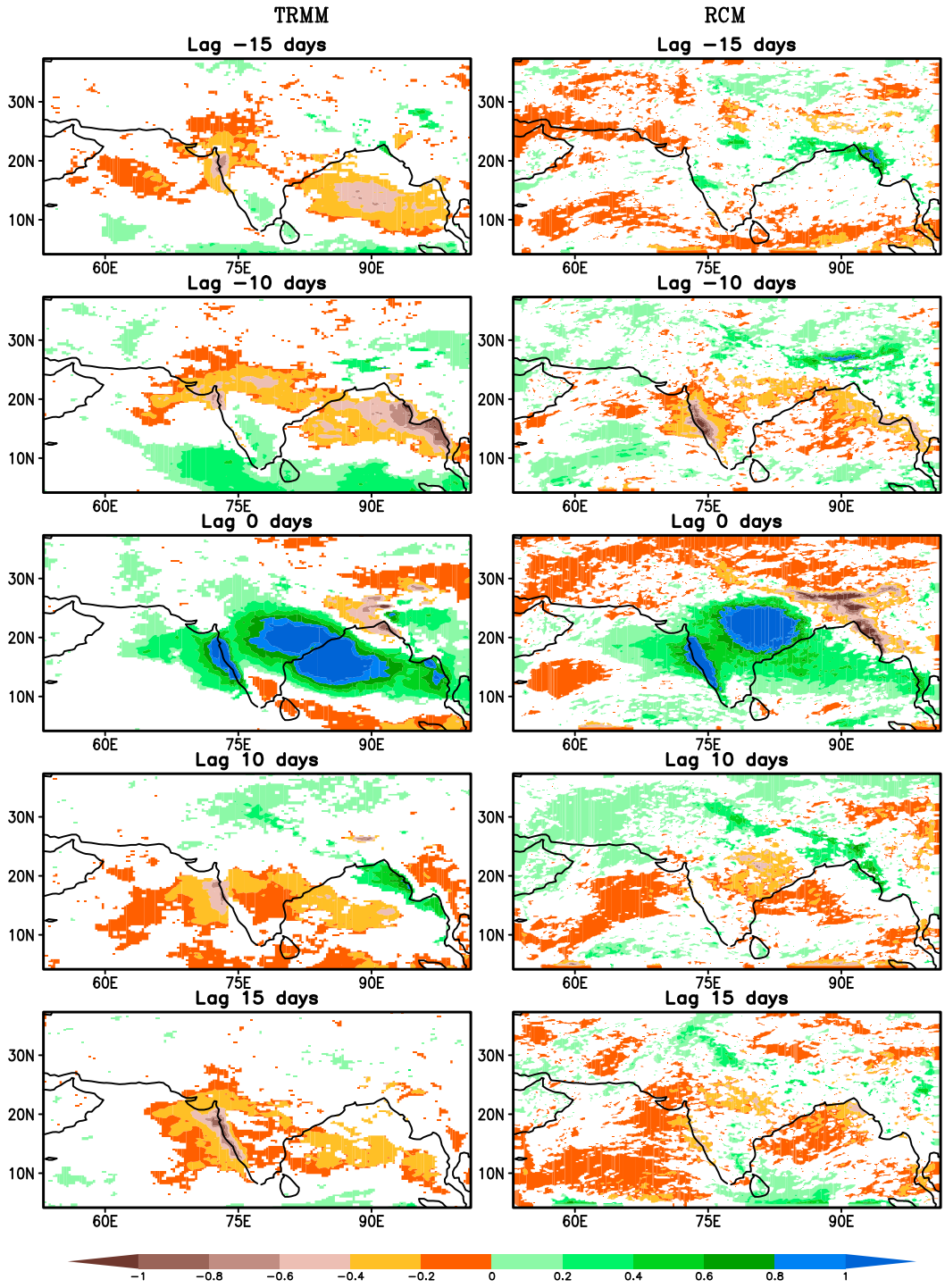

FIG. 7. The regression of daily bandpass (20–90 days)-filtered precipitation anomalies with corresponding central Indian bandpass-filtered precipitation anomalies from (left) observations (TRMM) and (right) the RCM simulation. The negative (positive) lags suggest that central Indian rainfall anomalies lead (lag) the rainfall anomaly. Only values significant at the 5% significance level according to a *t* test are plotted.

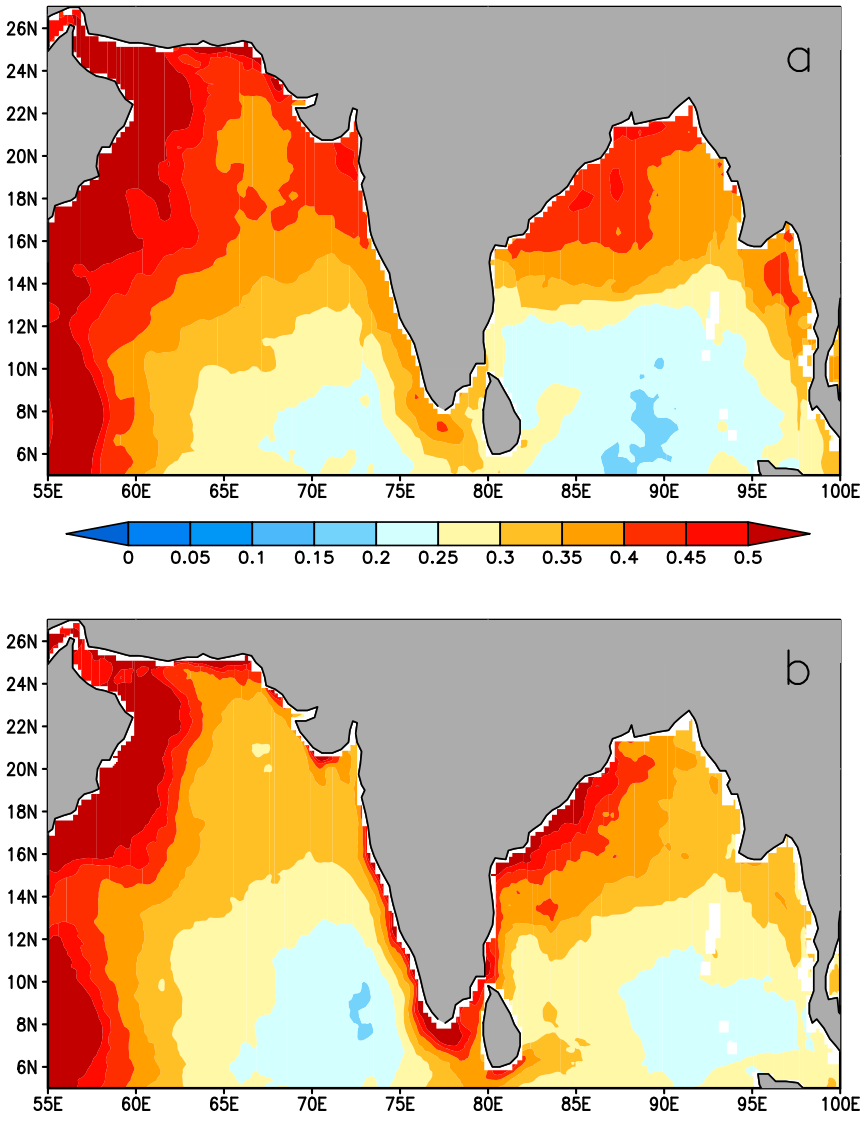

FIG. 8. The standard deviation of the intraseasonal (20–90-day filtered) SST anomalies (°C) from (a) observations (OSTIA; see Table 2) and (b) the RCM simulation.

with a corresponding increase (reduction) in low cloud cover over the BoB and the AS during active (inactive) periods of the ISM (not shown). The anomalies of the longwave flux (Figs. 9k,l) are much smaller, with a tendency to warm (cool) the ocean surface during wet (dry) spells of the ISM.

e. Intraseasonal anomalies of the subsurface ocean

In Fig. 10 we show the composites of the MLD, BLT, and depth of the 26° and 20°C isotherms for the wet and dry spells of the ISM. The SST changes on intraseasonal time scales in the BoB have been associated with changes to the MLD (Waliser et al. 2004; Keerthi et al. 2016; Li et al. 2016, 2017). In Figs. 10a,b we observed that the MLD over the BoB in the RCM tends to shoal during wet spells and deepen during dry spells of the ISM. Li et al. (2017) also found from observations that the freshwater flux of the ISM gives rise to a shallow MLD and a thick barrier layer. This is consistent with the increase in buoyancy flux during a dry spell resulting from an increased net heat flux (Fig. 9b) despite the decrease in the freshwater flux. However, in the AS the wind stirring influence and the Ekman pumping variations of the southern flank of the Findlater jet are the primary mechanisms for MLD variations (Murtugudde et al. 2007; Keerthi et al. 2016). In the RCM simulation we find that the southwesterlies over the AS are stronger during the wet spell (Fig. 4b), which increases the wind

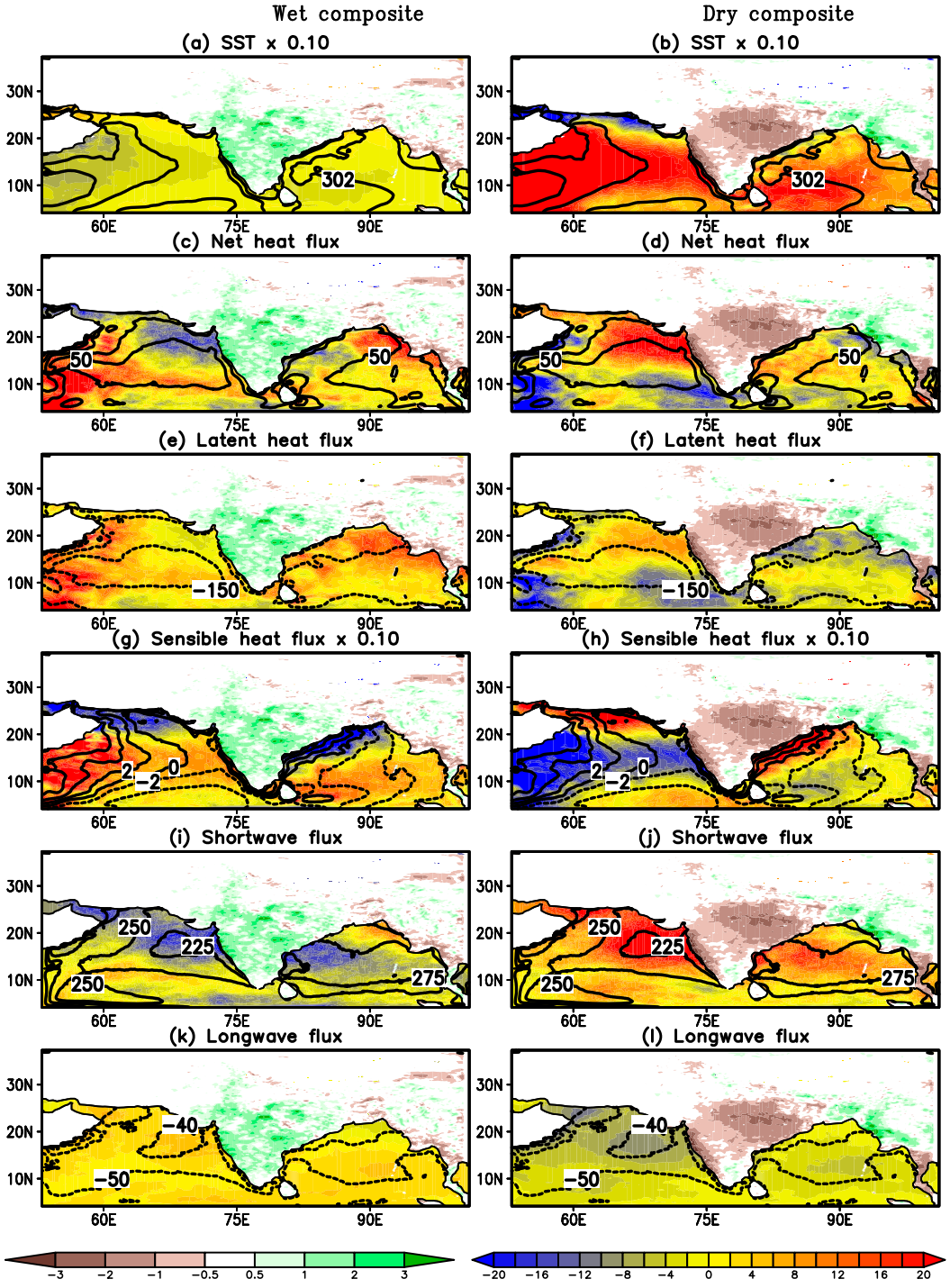

FIG. 9. The composite (left) wet and (right) dry intraseasonal ISM anomalies (color shaded) of (a),(b) SST (× 0.1°C); (c),(d) net heat flux; (e),(f) latent heat flux; (g),(h) sensible heat flux (× 0.1); (i),(j) net shortwave flux; and (k),(l) net longwave flux at the surface (all fluxes have units of W m^{-2}). Positive (negative) flux values (of either anomaly or climatology) denote the downward (upward) direction (away from) the ocean surface. The seasonal JJAS climatological mean values of the respective variables are contoured. The corresponding intraseasonal terrestrial precipitation anomalies over central India (mm day^{-1}) are also plotted.

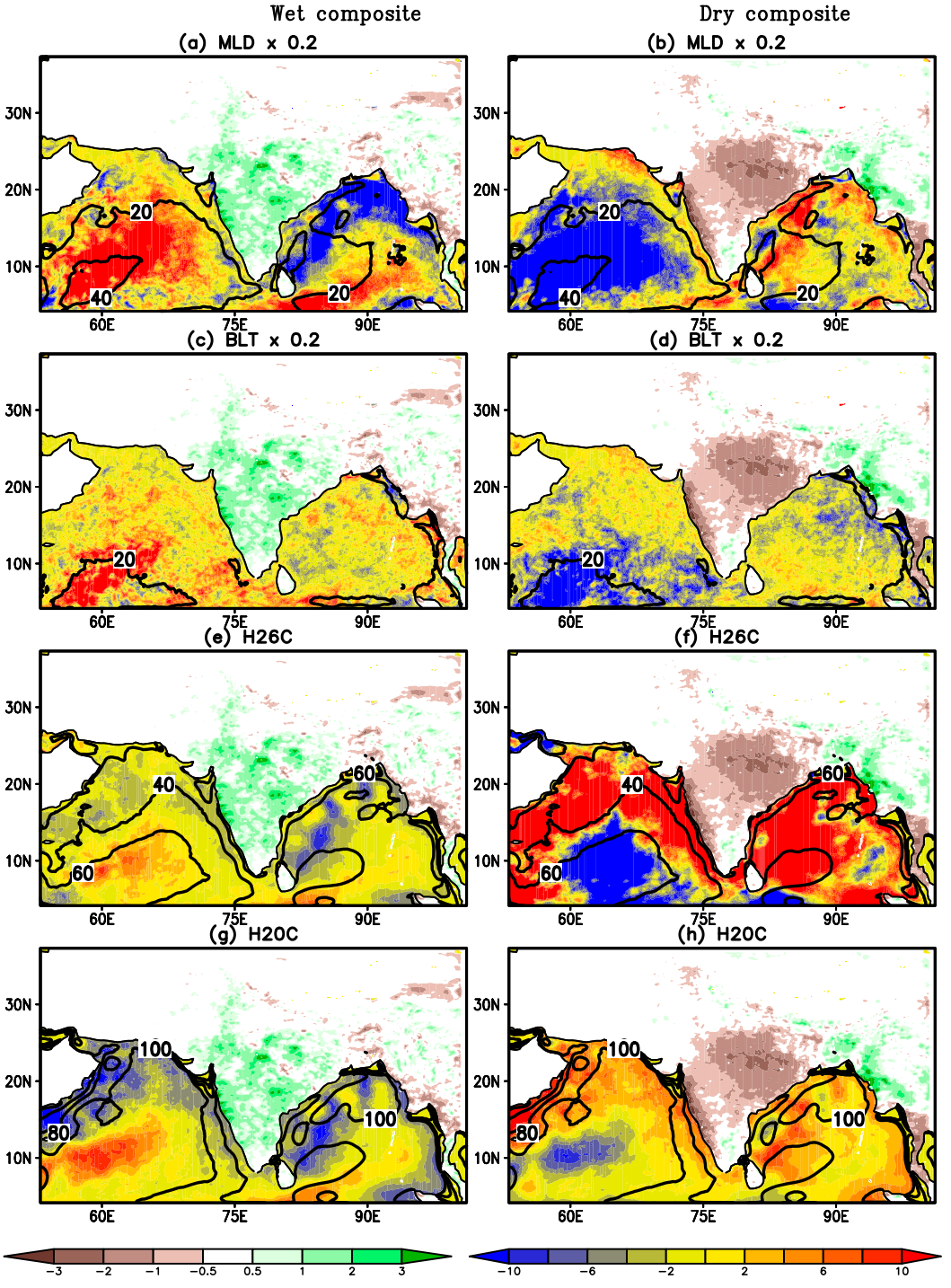

FIG. 10. The composite anomalies (m) of the (a),(b) MLD (× 0.2); (c),(d) BLT (× 0.2); (e),(f) depth of the 26°C isotherm (H26C); and (g),(h) depth of the 20°C isotherm (H20C) for (left) wet and (right) dry spells of the ISM. The corresponding seasonal JJAS climatological mean values of the respective variables are contoured in each panel with the corresponding terrestrial intraseasonal precipitation anomalies over central India (mm day^{-1}).

stirring effect represented by the friction velocity (Niiler and Kraus 1977). This results in the increased MLD during wet spells relative to dry spells over the AS despite the comparative reduction in surface heat flux. Keerthi et al. (2016) observed the Ekman pumping effect to be rather localized to the core of the Findlater jet region in the AS.

The relative asymmetry in the intraseasonal anomalies of SST, with larger positive anomalies during dry spells of the ISM and smaller negative anomalies in the wet spells, is consistent with the corresponding anomalies of the MLD. With a thicker MLD during dry spells, the SST anomalies have a tendency to grow with sustained surface heat flux forcing under relatively clear skies. But during wet spells with a smaller MLD, the SST anomalies have less time to grow before the surface flux anomalies change their sign as a result of the modulation of the atmospheric convection.

Changes in the BLT (Figs. 10c,d) are much smaller but still show a tendency toward thickening (thinning) during wet (dry) spells of the ISM. This is also a result of the model simulation lacking the input of river discharge, which is significant in the BoB (Vinayachandran et al. 2002). The effect of the BLT is subtle but important, as noted by Li et al. (2017), who observed that the input of freshwater flux at times of shallow MLD increases the mixed layer response to surface flux forcing from suppression of ocean entrainment from thicker BLT. This enhances the intraseasonal SST variations. Consequently, we find in the RCM simulation that the frequency of longer dry spells (those lasting longer than one pentad) is higher than corresponding wet spells because of the comparatively deeper MLD. This tendency of longer dry spells was also noted in the observational study of Pai et al. (2016).

The depth of the 26°C isotherm represents the tropical cyclone heat potential (Shay et al. 2000), and in the tropical Indian Ocean it also represents major seasonal variability (Jana et al. 2015) and intraseasonal variations (Krishnamurti et al. 2017). Figures 10e,f essentially show the same trend as the MLD, with deeper (shallower) anomalies during dry spells in the BoB (AS). Similarly, the depth of the 20°C isotherm that is usually used as a proxy for ocean heat content in the tropics shows similar positive (negative) anomalies in the BoB (AS).

f. Temporal coupling of the atmosphere, ocean surface, and subsurface ocean

The air–sea coupling is also understood from the diagnosis of the lead–lag correlation between atmospheric and oceanic variables (Cayan 1992; Wu et al. 2006; Misra 2008). In Figs. 11a and 11b we show the lead–lag correlation of intraseasonal precipitation anomalies with corresponding intraseasonal anomalies of SST from observations and the RCM simulation averaged over the BoB (85°–95°E and 5°–20°N) and the AS (63°–73°E and 5°–20°N), respectively. The positive (negative) correlations when precipitation lags (leads) SST suggest that the latter is driving the atmosphere (Wu et al. 2006; Misra 2008). In both regions, the SST is clearly seen leading (lagging) precipitation with maximum (minimum) correlation in both the BoB and the AS with around 10 and 5 days lead time in the observations in Figs. 11a and 11b, respectively. This temporal phase locking of precipitation and SST is well captured in the RCM simulation (Figs. 11a,b). In fact, Roxy et al. (2013) noted the faster interaction time scales of the SST and precipitation in the AS relative to the BoB and attributed it primarily to the presence of strong zonal gradients of SST in the AS that promote stronger convergence and vertical acceleration of moist air.

Similarly, the lead–lag correlations of SST with the subsurface ocean reveal a robust coupling in the RCM simulation. For example, the maximum negative correlation of SST with the MLD at a lag of around three days in both ocean basins suggest that thinning (thickening) of the MLD leads to warm (cold) SST anomalies (Figs. 11a,b). This is consistent with previous observational studies (Parampil et al. 2010; Li et al. 2016). On the other hand, the BLT in the RCM simulation in both ocean basins thins (thickens) after warm (cold) SST anomalies appear with a lag of around three days. This is consistent with the lead–lag relationship between precipitation and SST that allows for rainfall to freshen the ocean surface after warm SST anomalies appear. The correlations of the SST anomalies with depth of the 26° and 20°C isotherms are insignificant in the BoB but are significant in the AS with SST variations leading the relationship. Finally, the RCM simulation also shows that the net atmospheric heat flux leads the SST variation by about five days, which follows the observed relationship (Sengupta et al. 2001).

5. Conclusions

In this study, we conduct an analysis of the ISV from a coupled ocean–atmosphere RCM run at 10-km grid resolution for a period of 10 years (1986–95). This RCM integration is unprecedented in its spatial resolution and period of integration for the ISM. Hence, it allows us to better understand the coupled ISV. While there is a growing number of observational studies examining the intraseasonal variability of the ISM, they are limited by the sample size of specialized field observations (e.g., BOBMEX; Bhat 2002), by the coverage of the

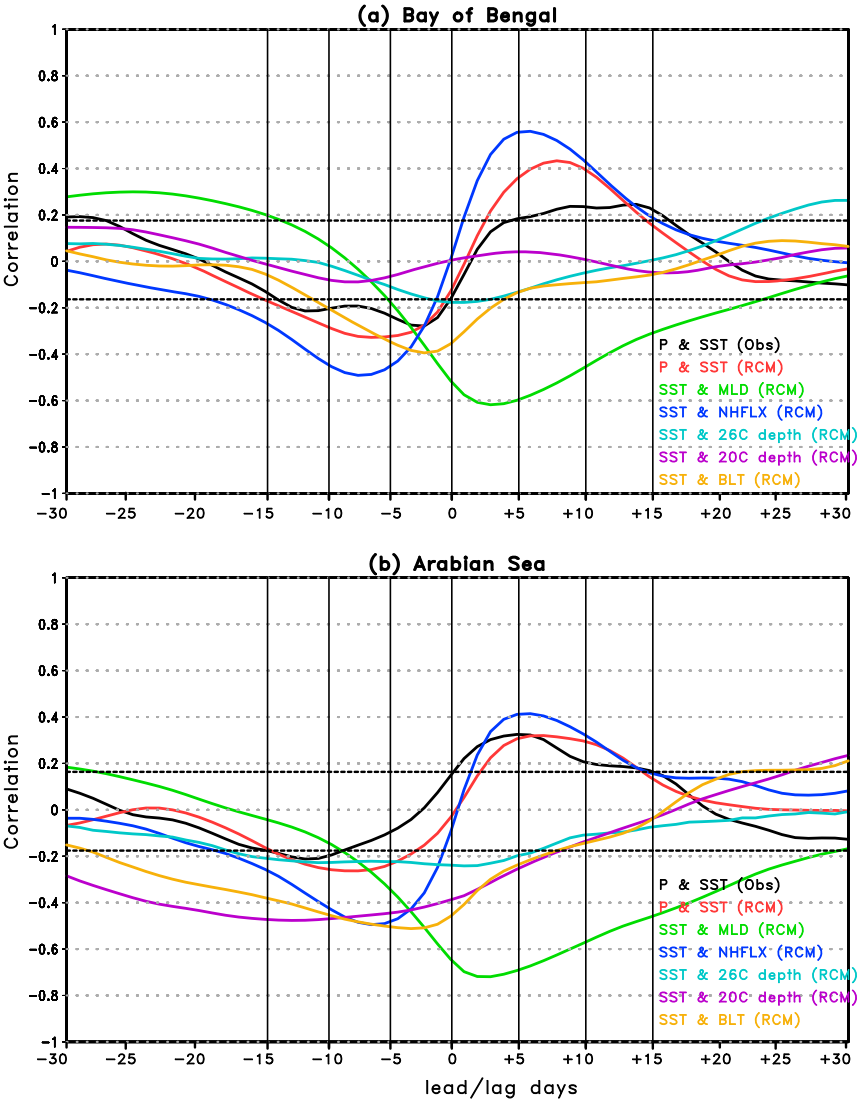

FIG. 11. Lead–lag correlation of precipitation (P) with SST (from observations and RCM) and SST with MLD, net atmospheric heat flux (NHFLX), depth of the 26°C isotherm (26C depth), depth of the 20°C isotherm (20C depth), and BLT from the RCM simulation for (a) Bay of Bengal (85°–95°E and 5°–20°N) and (b) Arabian Sea (63°–73°E and 5°–20°N). Positive (negative) lead time in days along the x axis indicates that the first variable is lagging (leading) the second variable shown in the legend. The bold dashed horizontal lines signify the 95% confidence interval according to a t test.

observations (e.g., limited ARGO floats with a five-day repeat cycle; Parampil et al. 2010), and by the analysis of observations conducted with uncoupled data assimilation models.

The RCM simulation in this study demonstrates reasonable fidelity in simulating the ISV precipitation. The wet and dry spells of the ISM are isolated by the 20–90-day bandpass-filtered precipitation anomalies over central India. The spatial features of the simulated intraseasonal rainfall anomalies, its temporal spectrum, and propagating characteristics show good fidelity. There are, however, some apparent biases of the RCM simulation including a dry bias of rainfall over the BoB during the wet spells.

Our analysis of the RCM simulation reveals that wet (dry) spells of the ISM are coincident with cooling (warming) anomalies across the AS and the BoB. This is consistent with some of the previous observational studies (Sengupta and Ravichandran 2001; Bhat 2002). These warm (cold) SST anomalies are compatible with the forcing of positive (negative) heat flux anomalies on the ocean surface, especially over the BoB, as has been

suggested by other observational studies (Bhat 2002; Parampil et al. 2010; Li et al. 2017). We also find robust intraseasonal variations of the MLD and the depths of the 26° and 20°C isotherms in the RCM simulation. The simulation shows shoaling (deepening) in the BoB of all of these depths during wet (dry) spells of the ISM. This finding is corroborated in Li et al. (2017). The success of this RCM simulation clearly establishes the importance of air–sea coupling for the simulation of the ISV, especially when the subsurface ocean also displays robust variations. Also, a reasonable stratification of the upper ocean is critical for sustaining intraseasonal features of the SST both in the BoB and the AS. The dry bias displayed by the RCM simulation during wet spells over the BoB is likely related to the excess shoaling of the MLD that enables the SST to respond far too rapidly to the surface fluxes thereby modulating the overlying atmospheric convection. But it also simulates the observed feature of having slightly longer dry spells than wet spells for the same reason. It is important to note that the absence of river discharge in the RCM is likely affecting the BLT and the MLD in our simulation. The presence of river discharge could possibly reduce the entrainment into the mixed layer during the wet spells and thereby sustain the SST anomalies longer and reduce the dry bias of the RCM. The importance of the river discharge on upper-ocean stratification and its feedback in the coupled system of the East Asian monsoon system is amply demonstrated in an earlier study (Ham et al. 2012).

The amplitude, the northwest–southeast tilt, and the relatively faster phase speed of the northward propagation of the ISV are seen as major improvements of the RCM simulation in comparison to some of the recent simulations of global coupled models at coarser spatial resolutions (Wang et al. 2009; Sharmila et al. 2013; Roxy et al. 2013). We believe that the spatial resolution of the RCM at 10 km may be one of the reasons for this improvement. We will investigate the sensitivity of the ISV to resolution and other parameters of the RCM in a future study.

Acknowledgments. The authors thank the two anonymous reviewers and Tracy Ippolito of the Center for Ocean-Atmospheric Prediction Studies, FSU, in assisting with the editorial revisions of the paper. The authors gratefully acknowledge the financial support given by NOAA (NA12OAR4310078) and the Earth System Science Organization, Ministry of Earth Sciences, Government of India (Grant MM/SERP/FSU/2014/SSC-02/002) to conduct this research under the Monsoon Mission. The supercomputing facility provided by XSEDE under Grant ATM10010 was used to complete the model integrations used in this study.

REFERENCES

Abhik, S., P. Mukhopadhyay, R. P. M. Krishna, K. D. Salunke, A. R. Dhakate, and S. A. Rao, 2016: Diagnosis of boreal summer intraseasonal oscillation in high resolution NCEP climate forecast system. *Climate Dyn.*, **46**, 3287–3303, https://doi.org/10.1007/s00382-015-2769-9.

Adler, R. F., G. J. Huffman, D. T. Bolvin, S. Curtis, and E. J. Nelkin, 2000: Tropical rainfall distributions determined using TRMM combined with other satellite and rain gauge information. *J. Appl. Meteor.*, **39**, 2007–2023, https://doi.org/10.1175/1520-0450(2001)040<2007:TRDDUT>2.0.CO;2.

Akhil, V. P., and Coauthors, 2014: A modeling study of the processes of surface salinity seasonal cycle in the Bay of Bengal. *J. Geophys. Res. Oceans*, **119**, 3926–3947, https://doi.org/10.1002/2013JC009632.

Alpert, J. C., M. Kanamitsu, P. M. Caplan, J. G. Sela, G. White, and E. Kalnay, 1988: Mountain induced gravity wave drag parameterization in the NMC medium-range forecast model. *Proc. 8th Conf. on Numerical Weather Prediction*, Baltimore, MD, Amer. Meteor. Soc., 726–733.

Bhat, G. S., 2002: Near-surface variations and surface fluxes over the northern Bay of Bengal during the 1999 Indian summer monsoon. *J. Geophys. Res.*, **107**, 4336, https://doi.org/10.1029/2001JD000382.

Carton, J. A., and B. S. Giese, 2008: A reanalysis of ocean climate using Simple Ocean Data Assimilation (SODA). *Mon. Wea. Rev.*, **136**, 2999–3017, https://doi.org/10.1175/2007MWR1978.1.

Cayan, D. R., 1992: Latent and sensible heat flux anomalies over the northern oceans: Driving the sea surface temperature. *J. Phys. Oceanogr.*, **22**, 859–881, https://doi.org/10.1175/1520-0485(1992)022<0859:LASHFA>2.0.CO;2.

Chou, M. D., and M. J. Suarez, 1994: An efficient thermal infrared radiation parameterization for use in general circulation models. NASA Tech. Memo. NASA-TM-104606, Vol. 3, 98 pp., https://ntrs.nasa.gov/archive/nasa/casi.ntrs.nasa.gov/19950009331.pdf.

——, K. T. Lee, S. C. Tsay, and Q. Fu, 1999: Parameterization for cloud longwave scattering for use in atmospheric models. *J. Climate*, **12**, 159–169, https://doi.org/10.1175/1520-0442-12.1.159.

Dash, S. K., M. S. Shekhar, and G. P. Singh, 2006: Simulation of Indian summer monsoon circulation and rainfall using RegCM3. *Theor. Appl. Climatol.*, **86**, 161–172, https://doi.org/10.1007/s00704-006-0204-1.

Donlon, C. J., M. Martin, J. D. Stark, J. Roberts-Jones, E. Fiedler, and W. Wimmer, 2012: The operational sea surface temperature and sea ice analysis (OSTIA). *Remote Sens. Environ.*, **116**, 140–158, https://doi.org/10.1016/j.rse.2010.10.017.

Ek, M. B., K. E. Mitchell, Y. Lin, E. Rogers, P. Grunmann, V. Koren, G. Gayno, and J. D. Tarpley, 2003: Implementation of Noah land surface model advances in the National Centers for Environmental Prediction operational mesoscale Eta model. *J. Geophys. Res.*, **108**, 8851, https://doi.org/10.1029/2002JD003296.

Gelaro, R., and Coauthors, 2017: The Modern-Era Retrospective Analysis for Research and Applications, version 2 (MERRA-2). *J. Climate*, **30**, 5419–5454, https://doi.org/10.1175/JCLI-D-16-0758.1.

Goswami, B. N., and P. K. Xavier, 2003: Potential predictability and extended range prediction of Indian summer monsoon breaks. *Geophys. Res. Lett.*, **30**, 1966, https://doi.org/10.1029/2003GL017810.

——, D. Sengupta, and G. S. Kumar, 1998: Intraseasonal oscillations and interannual variability of surface winds over the

Indian monsoon region. *J. Earth Syst. Sci.*, **107**, 45–64, https://doi.org/10.1007/BF02842260.

Guillemin, E. A., 1957: *Synthesis of Passive Networks*. Wiley, 571 pp.

Haidvogel, D. B., H. G. Arango, K. Hedstrom, A. Beckmann, P. Malanotte-Rizzoli, and A. F. Shchepetkin, 2000: Model evaluation experiments in the North Atlantic basin: Simulations in nonlinear terrain-following coordinates. *Dyn. Atmos. Oceans*, **32**, 239–281, https://doi.org/10.1016/S0377-0265(00)00049-X.

Ham, S., S.-Y. Hong, Y. Noh, S.-I. An, Y.-H. Byun, H.-S. Kang, J. Lee, and W.-T. Kwon, 2012: Effects of freshwater runoff on a tropical Pacific climate in the HadGEM2. *Asia-Pac. J. Atmos. Sci.*, **48**, 457–463, https://doi.org/10.1007/s13143-012-0041-3.

——, K. Yoshimura, and H. Li, 2016: Historical dynamical downscaling for East Asia with the Atmosphere and Ocean Coupled Regional Model. *J. Meteor. Soc. Japan*, **94A**, 199–208, https://doi.org/10.2151/jmsj.2015-046.

Hong, S. Y., and H. L. Pan, 1996: Nonlocal boundary layer vertical diffusion in a medium-range forecast model. *Mon. Wea. Rev.*, **124**, 2322–2339, https://doi.org/10.1175/1520-0493(1996)124<2322:NBLVDI>2.0.CO;2.

Huffman, G. J., R. F. Adler, B. Rudolf, U. Schneider, and P. R. Keehn, 1995: Global precipitation estimates based on a technique for combining satellite-based estimates, rain gauge analysis, and NWP model precipitation information. *J. Climate*, **8**, 1284–1295, https://doi.org/10.1175/1520-0442(1995)008<1284:GPEBOA>2.0.CO;2.

——, and Coauthors, 1997: The global precipitation climatology project (GPCP) combined precipitation dataset. *Bull. Amer. Meteor. Soc.*, **78**, 5–20, https://doi.org/10.1175/1520-0477(1997)078<0005:TGPCPG>2.0.CO;2.

——, R. F. Adler, D. T. Bolvin, and E. J. Nelkin, 2010: The TRMM Multi-Satellite Precipitation Analysis (TMPA). *Satellite Rainfall Applications for Surface Hydrology*, M. Gebremichael and F. Hossain, Eds., Springer, 3–22.

Jana, S., A. Gangopadhyay, and A. Chakraborty, 2015: Impact of seasonal river input on the Bay of Bengal simulation. *Cont. Shelf Res.*, **104**, 45–62, https://doi.org/10.1016/j.csr.2015.05.001.

Jiang, X., and Coauthors, 2011: Vertical diabatic heating structure of the MJO: Intercomparison between recent reanalyses and TRMM estimates. *Mon. Wea. Rev.*, **139**, 3208–3223, https://doi.org/10.1175/2011MWR3636.1.

Juang, H.-M., and M. Kanamitsu, 1994: The NMC nested regional spectral model. *Mon. Wea. Rev.*, **122**, 3–26, https://doi.org/10.1175/1520-0493(1994)122<0003:TNNRSM>2.0.CO;2.

Kanamitsu, M., W. Ebisuzaki, J. Woollen, S. K. Yang, J. J. Hnilo, M. Fiorino, and G. L. Potter, 2002: NCEP–DOE AMIP-II Reanalysis (R-2). *Bull. Amer. Meteor. Soc.*, **83**, 1631–1643, https://doi.org/10.1175/BAMS-83-11-1631.

Keerthi, M. G., M. Lengaigne, K. Drushka, J. Vialard, C. De Boyer Montegut, S. Pous, M. Levy, and P. M. Muraleedharan, 2016: Intraseasonal variability of mixed layer depth in the tropical Indian Ocean. *Climate Dyn.*, **46**, 2633–2655, https://doi.org/10.1007/s00382-015-2721-z.

Krishnamurthy, V., 2016: Tropical intraseasonal oscillations in CFSv2 during boreal summer and winter. *Int. J. Climatol.*, **37**, 3674–3693, https://doi.org/10.1002/joc.4948.

——, and J. Shukla, 2000: Intraseasonal and interannual variability of rainfall over India. *J. Climate*, **13**, 4366–4377, https://doi.org/10.1175/1520-0442(2000)013<0001:IAIVOR>2.0.CO;2.

——, and J. L. Kinter III, 2003: The Indian monsoon and its relation to global climate variability. *Global Climate*, X. Rodó and F. A. Comín, Eds., Springer, 186–236.

——, and J. Shukla, 2007: Intraseasonal and seasonally persisting patterns of Indian monsoon rainfall. *J. Climate*, **20**, 3–20, https://doi.org/10.1175/JCLI3981.1.

Krishnamurti, T. N., and D. Subrahmanyam, 1982: The 30–50 day mode at 850 mb during MONEX. *J. Atmos. Sci.*, **39**, 2088–2095, https://doi.org/10.1175/1520-0469(1982)039<2088:TDMAMD>2.0.CO;2.

——, M. Subramaniam, G. Daughenbaugh, D. Oosterhof, and J. Xue, 1992: One-month forecasts of wet and dry spells of the monsoon. *Mon. Wea. Rev.*, **120**, 1191–1223, https://doi.org/10.1175/1520-0493(1992)120<1191:OMFOWA>2.0.CO;2.

——, S. Jana, R. Krishnamurti, V. Kumar, R. Deepa, F. Papa, M. A. Bourassa, and M. M. Ali, 2017: Monsoonal intraseasonal oscillations in the ocean heat content over the surface layers of the Bay of Bengal. *J. Mar. Syst.*, **167**, 19–32, https://doi.org/10.1016/j.jmarsys.2016.11.002.

Large, W. G., J. C. McWilliams, and S. C. Doney, 1994: Oceanic vertical mixing: A review and a model with a nonlocal boundary layer parameterization. *Rev. Geophys.*, **32**, 363–403, https://doi.org/10.1029/94RG01872.

Lawrence, D. M., and P. J. Webster, 2002: The boreal summer intraseasonal oscillation: Relationship between northward and eastward movement of convection. *J. Atmos. Sci.*, **59**, 1593–1606, https://doi.org/10.1175/1520-0469(2002)059<1593:TBSIOR>2.0.CO;2.

Li, H., and V. Misra, 2014: Thirty-two-year ocean–atmosphere coupled downscaling of global reanalysis over the Intra-American Seas. *Climate Dyn.*, **43**, 2471–2489, https://doi.org/10.1007/s00382-014-2069-9.

Li, Y., W. Han, W. Wang, and M. Ravichandran, 2016: Intraseasonal variability of SST and precipitation in the Arabian Sea during Indian summer monsoon: Impact of ocean mixed layer depth. *J. Climate*, **29**, 7889–7910, https://doi.org/10.1175/JCLI-D-16-0238.1.

——, ——, ——, ——, T. Lee, and T. Shinoda, 2017: Bay of Bengal salinity stratification and Indian summer monsoon intraseasonal oscillation: 2. Impact on SST and convection. *J. Geophys. Res. Oceans*, **122**, 4312–4328, https://doi.org/10.1002/2017JC012692.

Lin, J. L., K. M. Weickman, G. N. Kiladis, B. E. Mapes, S. D. Schubert, M. J. Suarez, J. T. Bacmeister, and M. I. Lee, 2008: Subseasonal variability associated with Asian summer monsoon simulated by 14 IPCC AR4 coupled GCMs. *J. Climate*, **21**, 4541–4567, https://doi.org/10.1175/2008JCLI1816.1.

Mellor, G. L., and T. Yamada, 1982: Development of a turbulence closure model for geophysical fluid problems. *Rev. Geophys.*, **20**, 851–875, https://doi.org/10.1029/RG020i004p00851.

Misra, V., 2008: Coupled interactions of the monsoons. *Geophys. Res. Lett.*, **35**, L12705, https://doi.org/10.1029/2008GL033562.

——, P. Pantina, S. C. Chan, and S. DiNapoli, 2012: A comparative study of the Indian summer monsoon hydroclimate and its variations in three reanalyses. *Climate Dyn.*, **39**, 1149–1168, https://doi.org/10.1007/s00382-012-1319-y.

——, A. Mishra, and A. Bhardwaj, 2017: High-resolution regional-coupled ocean–atmosphere simulation of the Indian summer monsoon. *Int. J. Climatol.*, **37**, 717–740, https://doi.org/10.1002/joc.5034.

Molod, A., L. Takacs, M. Suarez, and J. Bacmeister, 2015: Development of the GEOS-5 atmospheric general circulation model: Evolution from MERRA to MERRA2. *Geosci. Model Dev.*, **8**, 1339–1356, https://doi.org/10.5194/gmd-8-1339-2015.

Moorthi, S., and M. J. Suarez, 1992: Relaxed Arakawa–Schubert: A parameterization of moist convection for general circulation

models. *Mon. Wea. Rev.*, **120**, 978–1002, https://doi.org/10.1175/1520-0493(1992)120<0978:RASAPO>2.0.CO;2.

Murtugudde, R., R. Seager, and P. Thoppil, 2007: Arabian Sea response to monsoon variations. *Paleoceanography*, **22**, PA4217, https://doi.org/10.1029/2007PA001467.

Neena, J. M., D. Waliser, and X. Jiang, 2017: Model performance metrics and process diagnostics for boreal summer intraseasonal variability. *Climate Dyn.*, **48**, 1661–1683, https://doi.org/10.1007/s00382-016-3166-8.

Niiler, P. P., and E. B. Kraus, 1977: One-dimensional models of the upper ocean. Modelling and prediction of the upper layer of the ocean, E. B. Kraus, Ed., Pergamon Press, 143–172.

Pai, D. S., L. Sridhar, and M. R. Ramesh Kumar, 2016: Active and break events of Indian summer monsoon during 1901–2014. *Climate Dyn.*, **46**, 3921–3939, https://doi.org/10.1007/s00382-015-2813-9.

Parampil, S. R., A. Gera, M. Ravichandran, and D. Sengupta, 2010: Intraseasonal response of mixed layer temperature and salinity in the Bay of Bengal to heat and freshwater flux. *J. Geophys. Res.*, **115**, C05002, https://doi.org/10.1029/2009JC005790.

Raghavan, K., D. R. Sikka, S. V. Gujar, and J. Findlater, 1975: The influence of cross-equatorial flow over Kenya on the rainfall of western India. *Quart. J. Roy. Meteor. Soc.*, **101**, 1003–1005, https://doi.org/10.1002/qj.49710143019.

Raju, A., A. Parekh, J. S. Chowdary, and C. Gnanaseelan, 2015: Assessment of the Indian summer monsoon in the WRF regional climate model. *Climate Dyn.*, **44**, 3077–3100, https://doi.org/10.1007/s00382-014-2295-1.

Rao, S., and Coauthors, 2011: Modulation of SST, SSS over northern Bay of Bengal on ISO time scale. *J. Geophys. Res.*, **116**, C09026, https://doi.org/10.1029/2010JC006804.

Roxy, M., Y. Tanimoto, B. Preethi, P. Terray, and R. Krishnan, 2013: Intraseasonal SST-precipitation relationship and its spatial variability over the tropical summer monsoon region. *Climate Dyn.*, **41**, 45–61, https://doi.org/10.1007/s00382-012-1547-1.

Sengupta, D., and M. Ravichandran, 2001: Oscillations of Bay of Bengal sea surface temperature during the 1998 summer monsoon. *Geophys. Res. Lett.*, **28**, 2033–2036, https://doi.org/10.1029/2000GL012548.

——, B. N. Goswami, and R. Senan, 2001: Coherent intraseasonal oscillations of ocean and atmosphere during the Asian summer monsoon. *Geophys. Res. Lett.*, **28**, 4127–4130, https://doi.org/10.1029/2001GL013587.

Sharmila, S., and Coauthors, 2013: Role of ocean–atmosphere interaction on northward propagation of Indian summer monsoon intra-seasonal oscillations (MISO). *Climate Dyn.*, **41**, 1651–1669, https://doi.org/10.1007/s00382-013-1854-1.

Shay, L. K., G. Goni, and P. G. Black, 2000: Effects of a warm oceanic feature on Hurricane Opal. *Mon. Wea. Rev.*, **128**, 1366–1383, https://doi.org/10.1175/1520-0493(2000)128<1366:EOAWOF>2.0.CO;2.

Shchepetkin, A. F., and J. C. McWilliams, 2005: The regional oceanic modeling system (ROMS): A split-explicit, free-surface, topography-following-coordinate oceanic model. *Ocean Model.*, **9**, 347–404, https://doi.org/10.1016/j.ocemod.2004.08.002.

Shige, S., Y. Nakano, and M. K. Yamamoto, 2017: Role of orography, diurnal cycle, and intraseasonal oscillation in summer monsoon rainfall over the Western Ghats and Myanmar Coast. *J. Climate*, **30**, 9365–9381, https://doi.org/10.1175/JCLI-D-16-0858.1.

Sikka, D. R., and S. Gadgil, 1980: On the maximum cloud zone and the ITCZ over Indian longitudes during the southwest monsoon. *Mon. Wea. Rev.*, **108**, 1840–1853, https://doi.org/10.1175/1520-0493(1980)108<1840:OTMCZA>2.0.CO;2.

Sperber, K. R., and H. Annamalai, 2008: Coupled model simulations of boreal summer intraseasonal (30–50 day) variability, Part 1: Systematic errors and caution on use of metrics. *Climate Dyn.*, **31**, 345–372, https://doi.org/10.1007/s00382-008-0367-9.

——, ——, I. S. Kang, A. Kitoh, A. Moise, A. Turner, B. Wang, and T. Zhou, 2013: The Asian summer monsoon: An intercomparison of CMIP5 vs. CMIP3 simulations of the late 20th century. *Climate Dyn.*, **41**, 2711–2744, https://doi.org/10.1007/s00382-012-1607-6.

Tiedtke, M., 1983: The sensitivity of the time-mean large-scale flow to cumulus convection in the ECMWF model. *Proc. ECMWF Workshop on Convection in Large-Scale Models*, Reading, United Kingdom, European Centre for Medium-Range Weather Forecasts, 297–316.

Umakanth, U., A. P. Kesarkar, A. Raju, and S. V. B. Rao, 2016: Representation of monsoon intraseasonal oscillations in regional climate model: Sensitivity to convective physics. *Climate Dyn.*, **47**, 895–917, https://doi.org/10.1007/s00382-015-2878-5.

Umlauf, L., and H. Burchard, 2003: A generic length-scale equation for geophysical turbulence models. *J. Mar. Res.*, **61**, 235–265, https://doi.org/10.1357/002224003322005087.

Vecchi, G. A., and D. E. Harrison, 2002: Monsoon breaks and subseasonal sea surface temperature variability in the Bay of Bengal. *J. Climate*, **15**, 1485–1493, https://doi.org/10.1175/1520-0442(2002)015<1485:MBASSS>2.0.CO;2.

Vinayachandran, P. N., V. S. N. Murty, and V. Ramesh Babu, 2002: Observations of barrier layer formation in the Bay of Bengal during summer monsoon. *J. Geophys. Res.*, **107**, 8018, https://doi.org/10.1029/2001JC000831.

Waliser, D. E., 2006: Intraseasonal variability. *The Asian Monsoon*, B. Wang, Ed., Springer, 203–257.

——, Z. Zhang, K. M. Lau, and J. H. Kim, 2001: Interannual sea surface temperature variability and the predictability of tropical intraseasonal variability. *J. Atmos. Sci.*, **58**, 2596–2615, https://doi.org/10.1175/1520-0469(2001)058<2596:ISSTVA>2.0.CO;2.

——, R. Murtugudde, and L. E. Lucas, 2004: Indo-Pacific Ocean response to atmospheric intraseasonal variability: 2. Boreal summer and the Intraseasonal Oscillation. *J. Geophys. Res.*, **109**, C03030, https://doi.org/10.1029/2003JC002002.

Wang, B., and H. Rui, 1990: Synoptic climatology of transient tropical intraseasonal convection anomalies: 1975–1985. *Meteor. Atmos. Phys.*, **44**, 43–61, https://doi.org/10.1007/BF01026810.

——, and X. Xie, 1997: A model for the boreal summer intraseasonal oscillation. *J. Atmos. Sci.*, **54**, 72–86, https://doi.org/10.1175/1520-0469(1997)054<0072:AMFTBS>2.0.CO;2.

Wang, W., M. Chen, and A. Kumar, 2009: Impacts of ocean surface on the northward propagation of the boreal summer intraseasonal oscillation in the NCEP Climate Forecast System. *J. Climate*, **22**, 6561–6576, https://doi.org/10.1175/2009JCLI3007.1.

Webster, P. J., V. O. Magana, T. N. Palmer, J. Shukla, R. A. Tomas, M. U. Yanai, and T. Yasunari, 1998: Monsoons: Processes, predictability, and the prospects for prediction. *J. Geophys. Res.*, **103**, 14 451–14 510, https://doi.org/10.1029/97JC02719.

Wu, R., B. P. Kirtman, and K. Pegion, 2006: Local air–sea relationship in observations and model simulations. *J. Climate*, **19**, 4914–4932, https://doi.org/10.1175/JCLI3904.1.

Yasunari, T., 1979: Cloudiness fluctuations associated with the Northern Hemisphere summer monsoon. *J. Meteor. Soc. Japan*, **57**, 227–242.

Zhao, Q., and F. H. Carr, 1997: A prognostic cloud scheme for operational NWP models. *Mon. Wea. Rev.*, **125**, 1931–1953, https://doi.org/10.1175/1520-0493(1997)125<1931:APCSFO>2.0.CO;2.